https://dx.doi.org/10.1016/j.ensm.2021.08.011

Realizing wide-temperature Zn metal anodes through concurrent interface stability regulation and solvation structure modulation

Z. Hou, Z. Lu, Q. Chen, B. Zhang

Abstract: Stable cycling of Zn metal anodes under thermal extremes remains a grand challenge with the corresponding failure mechanisms largely unexplored. Here, we unravel the origin of thermal instability during Zn plating/stripping. The low temperature renders deteriorative dendrites growth, while a high temperature causes aggravating parasitic reactions. Zn metal/electrolyte interface and electrolyte solvation chemistry are then regulated via the introduction of oligomer poly(ethylene glycol) dimethyl ether as a competitive-solvent into the aqueous electrolyte to circumvent these issues. Complementary experimental and theoretical studies demonstrate that the competitive-solvent shifts water-occupied interface into oligomer one through preferential Zn surface adsorption, enabling dendrite-free Zn morphologies. Furthermore, such solvent alters the electrolyte interaction by re-constructing oligomer/water hydrogen bonds and participating in the solvation sheath of Zn ions, which highly alleviates parasitic reactions. Consequently, Zn metal anodes deliver over 1600 h Zn cyclic lifetime at all the tested temperatures of 0, 25 and 50 °C, over 10-fold enhancement than in pristine electrolytes. Application-wise, competitive-solvent suppresses the fast cathode dissolution because of highly reduced water activities and realizes the stable Zn/V_2O_5 full cells over a wide temperature range from -15 to 65 °C.

Keywords: Zn metal anodes, thermal instability, dendrites growth, parasitic reactions, competitive-solvent, wide-temperature

1. Introduction

Aqueous rechargeable batteries with economic, nontoxic and intrinsically nonflammable superiority are regarded as the reliable energy storage candidates to complement the conventional Li-ion batteries.[1] Zn metal anodes possess a high volumetric capacity of 5851 mAh/cm^3 and an appropriate redox potential of 0.76 V vs. the standard hydrogen electrode, making Zn-based batteries of particular interest among the aqueous energy technologies.[2-8] However, rechargeable Zn metal batteries' commercial application is highly plagued by the poor reversibility of Zn metal anodes during deposition/stripping process, which is primarily originated from the mutually reinforced issues of dendrites formation, chemical corrosion and hydrogen evolution reaction (HER).[9-14] Zn dendrites growth is induced by the nonuniform deposition, which would result in a short circuit of cells and safety hazards.[15-21] Besides, massive non-conductive metal oxides/hydroxides byproducts are gradually formed on the surface of Zn metal anodes due to the chemical corrosion with electrolytes and the generation of hydroxyl ion derived from HER.[22-25] These side reactions consume the active Zn metal and electrolytes, leading to a short cycle life. The resulted by-products further impede the homogeneity of Zn^{2+} transport, in turn facilitating dendrite growth. Furthermore, the accompanying gas evolution would lead to safety concerns due to pressure upsurge inside cells.

Considerable efforts have been proposed to overcome the above obstacles and stabilize Zn metal anodes.[14, 18, 19, 26-34] For example, organic additives that could be adsorbed on the electrodes surface, are developed to restrain Zn^{2+} 2D diffusion and homogenize Zn deposition.[30-32] Such adsorptive additives also help to alleviate corrosion reactions to a certain extent at room temperature. In addition, the introduction of foreign molecules into the electrolyte, which could involve the solvation of Zn^{2+}, is an effective approach to attenuate the interaction between water

molecules and Zn^{2+} for suppressing parasitic reactions.[18, 22, 35] Despite these stimulating achievements, implementing superior Zn metal anodes for long-term cycles is still challenging, probably due to the difficulties in simultaneously tackling the aforementioned several issues. More critically, most of the previous research is focused on enhancing the electrochemical performance of Zn metal anodes at room temperature.[9] The Zn deposition/stripping behavior under thermal extremes, especially at high temperatures, is rarely explored with the underlying failure mechanisms largely elusive.[35-37]

Herein, we first investigate the stability of Zn metal anodes at three different temperatures, i.e., 0, 25 and 50 °C, and reveal the harsh temperature-induced instability due to either the rampant dendrites growth at low temperatures or amplified parasitic reactions in Zn/electrolyte interfaces at high temperatures. To synchronously solve these challenges, a competitive-solvent oligomer poly(ethylene glycol) dimethyl ether (PEGDME) with multi-functions is proposed to realize wide-temperature Zn metal anodes through (1) passivating Zn metal anodes by rich polymer chains to regulate Zn deposition and resist corrosion; (2) constructing PEGDME-involved solvation sheath of Zn^{2+} induced by its strong solvation capability to restrain corrosion and HER; (3) disrupting the water/water hydrogen bonds due to excellent water solubility and ample ether groups, which decreases water activities and further suppresses side reactions. Additionally, such electrolyte is favorable for mitigating the dissolution of commercial V_2O_5 cathode and, in turn, enables the excellent Zn/V_2O_5 full cells over a wide temperature range from -15 to 65 °C.

2. Experimental section

2.1 Preparation of electrolytes and cathodes. Hybrid electrolytes were fabricated by dissolving 1 M zinc trifluoromethanesulfonate ($Zn(CF_3SO_3)_2$) in water/poly(ethylene glycol) dimethyl ether (PEGDME) binary solvents. The mass ratio of water to PEGDME was controlled to be 60:40, 50:50 and 40:60. For the sake of clarity, the above electrolytes were denoted as PEGDME-X, where "X" represents the mass proportion of PEGDME in electrolytes. 1 M $Zn(CF_3SO_3)_2$ in pure water was used as a control electrolyte, correspondingly marked as PEGDME-0. The V_2O_5 cathode slurry was prepared by mixing commercial 70 wt% vanadium(V) oxide (V_2O_5; Aldrich), 20 wt% Super P and 10 wt% polyvinylidene fluoride (PVDF) in N-methyl-2-pyrrolidone. The $LiMn_2O_4$ cathode slurry was obtained with the same procedure consisting of 80 wt% lithium manganese oxide ($LiMn_2O_4$; MTI), 10 wt% Super P and 10 wt% PVDF. These cathodes were fabricated by casting the corresponding slurries onto the stainless steel foils and then dried at 60 °C for 12 h.

2.2 Characterizations. The scanning electron microscope (SEM) (TESCAN MAIA3) was employed to collect the morphologies of cycled Zn metal anodes. FTIR and Raman measurements were respectively carried out on Shimadzu fourier transform infrared spectrometer and Witec-Confocal Raman system (UHTS 600 SMFC VIS) with a laser wavelength of 532 nm. X-ray diffraction (XRD) patterns were acquired using X-ray diffractometer (Rigaku SmartLab) with Cu Ka radiation. X-ray photoelectron spectroscopy (XPS) was recorded by X-ray photoelectron spectrometer (Nexsa) with Al Ka X-ray line. Solubilities of V_2O_5 electrodes in PEGDME-0 and PEGDME-50 were conducted by inductively coupled plasma mass spectrometry (ICP-MS). The homemade pressure sensor setup (Fig. S17a) was used to monitor the pressure variation in real-time where Zn foils were soaked in PEGDME-0 and PEGDME-50.

2.3 Electrochemical measurements. CR2032 coin-type cells were assembled and then tested on Land battery testing systems at various temperatures (-15, 0, 25, 50 and 65 °C). Glass fiber and PEGDME-X were used as separators and electrolytes, respectively. For deposition/stripping tests in Zn/Zn cells, 1 mAh/cm^2 of Zn was cycled repeatedly at 1 mA/cm^2. CE measurements were assessed with a fixed discharge capacity of 1 mAh/cm^2 and a charge cut-off voltage of 0.5 V at 1 mA/cm^2 in Cu/Zn cells. The CE was then calculated based on the capacity ratio of charge to discharge. Cyclic voltammetry (CV) curves and ionic conductivities of electrolytes were performed on the BioLogic electrochemical workstation (VSP). Ionic conductivities were obtained from electrochemical impedance spectroscopy (EIS, from 10^5 and 10^{-1} Hz and potential amplitude of 5 mV) using stainless steel/stainless steel cells. The calculation equation is σ = L/A*R, where R is the measured resistance, L is the distance between the electrodes and A is the area of the electrodes. The full cells with V_2O_5 cathodes were tested between 0.6 and 1.8 V, and the one coupled with $LiMn_2O_4$ cathodes were cycled between 1.4 and 2.1 V. To activate the V_2O_5 cathodes, Zn/V_2O_5 full cells were cycled at 20 mA/g for 10 cycles before testing at high current rates.

2.4 Computational methods. All computations were carried at the level of density functional theory and the setup was consistent with our previous study.[38-40] Briefly, to calculate the dissociation energy of isolated complexes, ORCA was used with the B3LYP hybrid functional and the cc-pVDZ basis set of Dunning was adopted.[41-44] A 6-coordinated Zn^{2+} configuration was chosen. For simplicity, the PEGDME was modeled using a two-segment model with 2 ether groups. The dissociation energy E_d of the complexes was calculated using:

$$\mathrm{E}_d^{Zn(H_2O)_4PEGDME^{2+}} = \mathrm{E}_{Zn^{2+}} + 4\mathrm{E}_{H_2O} + \mathrm{E}_{PEGDME} - \mathrm{E}_{Zn(H_2O)_4PEGDME^{2+}}$$

$$\mathrm{E}_d^{Zn(H_2O)_6{}^{2+}} = \mathrm{E}_{Zn^{2+}} + 6\mathrm{E}_{H_2O} - \mathrm{E}_{Zn(H_2O)_6{}^{2+}}$$

where $E_d^{Zn(H_2O)_6{}^{2+}}$, $E_d^{Zn(H_2O)_4PEGDME^{2+}}$, $E_{Zn^{2+}}$, E_{H_2O}, $E_{Zn(H_2O)_4PEGDME^{2+}}$, and $E_{Zn(H_2O)_6{}^{2+}}$ are the dissociation energies of the isolated $Zn(H_2O)_6^{2+}$ complex, the $Zn(H_2O)_4PEGDME^{2+}$ complex, the ground state energies of the Zn^{2+} cation, the H_2O molecule, the $Zn(H_2O)_6^{2+}$ complex, and the $Zn(H_2O)_4PEGDME^{2+}$ complex, respectively.

The *ab initio* molecular dynamics simulations (AIMD) and the adsoprtion energy calculations were carried out using periodic DFT.[45-47] Generalized gradient approximation (GGA) with the Perdew–Burke–Ernzerhof (PBE) functional was used. A planewave cutoff of 430 eV was adopted. For AIMD simulations, a Nose-Hoover thermobath was coupled to the simulated systems and the temperature was controlled at 300 K. The time step was chosen to be 1 fs. The simulation length was 20 ps for each system. For different systems, the simulations boxes were constructed differently. For the case of PEGDME-0, 29 water molecules, 1 Zn^{2+} cation, and 2 $CF_3SO^-_3$ anions were packed into a cubic simulation box and equilibration was carried out to achieve by controlling the pressure to 0.1 MPa before the actual production run using the NVT ensemble. Similarly, we also simulated the case PEGDME-50. 20 water molecules, 1 Zn^{2+} cation, 2 $CF_3SO^-_3$ anions, and one PEGDME were used. In order to keep the computational cost manageable, the PEGDME was modeled using a relatively short chain polymer containing 8 ether groups. The overall composition of PEGDME used in the current work is $CH_3(OCH_2CH_2)_7OCH_3$. To calculate the adoption energy and Zn (0001) surfaces were constructed using slab models. Each slab contains at least 4 layers of metal atoms as the substrate and a vacuum layer of 20Å to avoid self-interactions. The PEGDME was modeled using a $CH_3OCH_2CH_2OCH_3$ configuration. The adsorption energy E_{ad} was calculated using the following equation:

$$E_{ad} = E_{substrate-adsorbate} - E_{substrate} - E_{adsorbate}$$

where $E_{substrate-adsorbate}$, $E_{substrate}$, and $E_{adsorbate}$ are the energies of substrate-adsorbate complex, the substrate, and the isolated adsorbate, respectively.

3. Results and discussion

3.1 Zn deposition/stripping behavior at different temperatures

Our efforts are firstly devoted to understanding the Zn plating/stripping at various temperatures. The cycle and CE performance are respectively collected using Zn/Zn and Cu/Zn cells at 0, 25 and 50 °C in 1 M $Zn(CF_3SO_3)_2$ electrolyte. It is found that Zn/Zn cells present the best stability at room temperature. Specifically, cells could steadily run for ~175 h (25 °C), ~100 h (50 °C) and ~55 h (0 °C) (Fig. 1a). As shown in Fig. 1b and Fig. S1, a similar tendency persists in CE performance (84 cycles at 25 °C, 38 cycles at 50 °C and instability for all cycles at 0 °C).

The ionic conductivities at various temperatures are collected from electrochemical impedance spectroscopy (EIS) using stainless steel/stainless steel cells to unravel the reasons for the inferior performance under thermal extremes. As shown in Fig. 1c, ionic conductivity decreases as the temperature drops, which would facilitate dendrites initiation. The EIS and cyclic voltammetry (CV) curves using the Zn/Zn cells further confirm the increased resistance and slow electrochemical kinetics at low temperature (Fig. S2). These deteriorations trigger the uneven Zn deposition at low temperature, as seen from SEM images in Figs. S3a-c, in turn leading to the rapid short circuit of cells.[48]

The side reactions between the electrodes and the electrolytes are assumed to be responsible for the performance degradation at high temperatures.[49] The highest corrosive rate is found at 50 °C, as inferred by the linear polarization curves with a largest value of 28.22 uA (Fig. 1d). The phenomenon is also supported by the SEM images of Zn foil after soaking in the electrolyte for 72 h at various temperatures (Figs. 1f-h), where loose porous Zn with huge flakes is observed at 50 °C. In addition, high temperature causes deteriorative HER due to the increased water activities during

Zn deposition process, leading to abundant ZnO by-products formed on the surface of Zn metal (Fig. 1e). Such electrochemically inactive ZnO would contribute to the poor Zn reversibility.

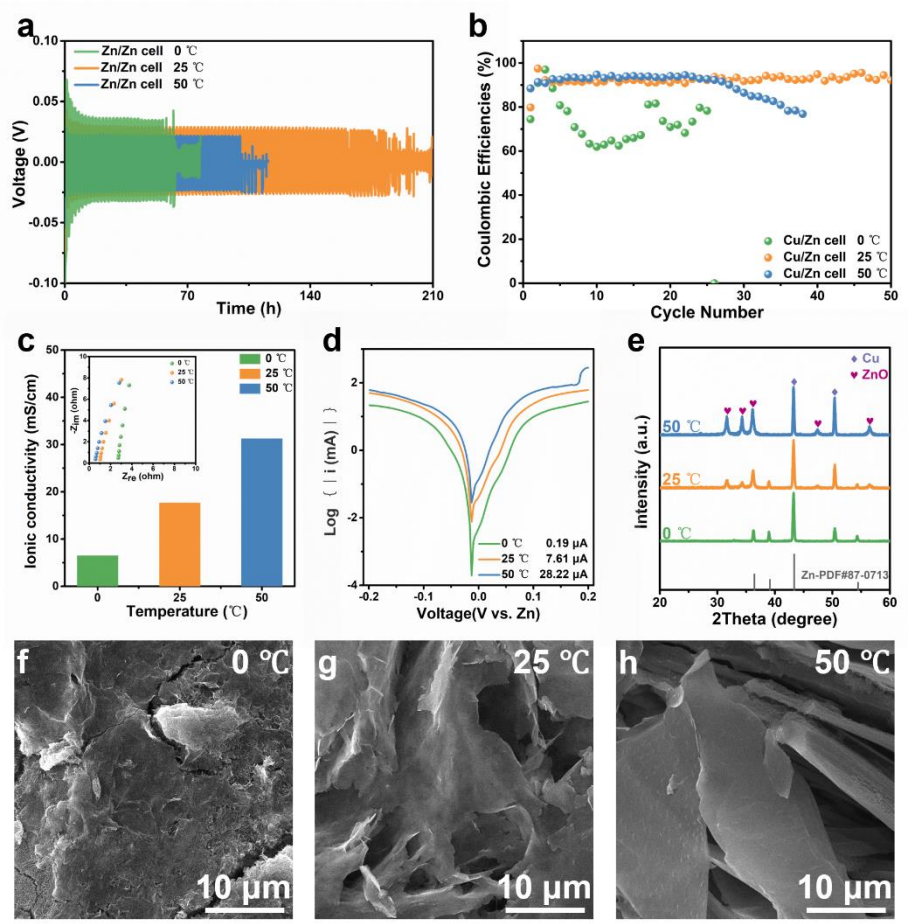

Fig. 1. The Zn deposition/stripping behavior under thermal extremes. (a) Cyclic performance of Zn/Zn cells and (b) CE performance of Cu/Zn cells at 0, 25 and 50 °C, at a current density of 1 mA/cm^2 and cycling capacity of 1 mAh/cm^2. (c) Ionic conductivities and (d) linear polarization curves related to chemical corrosion at 0, 25 and 50 °C. (e) XRD patterns of Cu foils with 4 mAh/cm^2 of Zn deposition at 1 mA/cm^2 at 0, 25 and 50 °C. SEM images of Zn foils after soaking in the electrolyte for 72 h at (f) 0 °C, (g) 25 °C and (h) 50 °C.

3.2 A competitive-solvent strategy and the underlying mechanism

We add an oligomer PEGDME (M_n=500) that could compete with water molecules into 1 M $Zn(CF_3SO_3)_2$ electrolyte to circumvent the dendrites growth at low temperatures and rampant parasitic reactions at high ones. It is expected that the polymer chains of PEGDME could adsorb on the electrode surface to regulate Zn deposition and shield the Zn metal from corrosion. The adsorb behavior is first confirmed by the smaller double layer capacitance in electrolyte with PEGDME than without it (Fig. S5a). To quantify the adsorptive feature of PEGDME to the anode surface, we compute the adsorption energy of PEGDME and H_2O to the Zn (0001) surface. As shown in Fig. S6a, the adsorption energy of PEGDME on Zn is -0.63 eV, whereas the value for H_2O is -0.12 eV, on the per molecule base. Such a result indicates that PEGDME may cover significant portion of Zn surface when added to the electrolyte. The *ab initio* molecular dynamics simulations (AIMD) simulations are further conducted to figure out the equilibrium structure of Zn surface in both pure H_2O and H_2O/PEGDME solutions. Once PEGDME is added as a competitive-solvent, the polymer chains compete with water molecules on the Zn surface and quickly replace them (Fig. 2a and Fig. S7), resulting in the coverage of Zn surface by PEGDME to a large extent.

It is known that PEGDME has abundant ether groups and strong solvation ability,[50, 51] so we conjecture it would change electrolyte solvation chemistry. To investigate the interaction among PEGDME, water and Zn^{2+}, FTIR and Raman measurements are carried out on a collection of samples, including water/PEGDME mixtures (denoted as W/P-X) and 1 M $Zn(CF_3SO_3)_2$ in water/PEGDME electrolytes (marked as PEGDME-X), where both "X" represents the mass ratio of PEGDME in the binary solvent systems. As shown in Fig. 2b, the H-O stretching vibration of water at 3000-3500 cm^{-1} moves to higher wavenumbers with increased PEGDME content in the W/P-X, as a result of the breakage of water/water hydrogen bonds (HBs) network by the newly

formed water/PEGDME HBs.[51, 52] This would significantly reduce free water molecules and water activities.[51] Furthermore, the FTIR spectra of W/P-X and corresponding PEGDME-X are compared to study the interplay between PEGDME and Zn^{2+}. As shown in Fig. 2c, the introduction of PEGDME leads to red drift of v_sSO_3 due to its participation in the solvation structure of Zn^{2+}. The blue shift of C-H stretching of PEGDME is detected after adding Zn salt into W/P-X, further implying the presence of strong interaction between PEGDME and Zn^{2+} (Fig. S8b). Similarly, these interplays are validated in Raman spectra (see Figs. S9 and S10 for details).

Theoretical calculations are employed to further understand the effect of PEGDME competitive-solvent on the microscopic structures of the electrolytes. First, we gather statistics on the HBs between H_2O molecules from AIMD simulations and the results are shown in Fig. 2d. In PEGDME-0, ~1.8 HBs are shared by each water molecule. In comparison, when PEGDME is added, the number of HBs between water molecules significantly drops to < 0.5 per molecule. The reason lies in that the high-concentration ether groups of the competitive PEGDME tend to coordinate with water molecules. In addition, we carried out AIMD simulations to acquire the equilibrium solvation structure. As shown in Figs. 2e and f, the 6-fold coordination of Zn^{2+} remained to be the major coordination mode after the addition of PEGDME. However, more than one oxygen atom is replaced by the ether group of competitive PEGDME in the first solvation sheath of Zn^{2+}. Such equilibrium structure further supports the experimental findings that competitive PEGDME has relatively strong solvation capability and could change the solvation structure of Zn^{2+}.

Chronoamperometry (CA) test could provide clues about the diffusion manner, which is obtained by applying constant cathodic overpotential for Zn reduction in PEGDME-0 and PEGDME-50. PEGDME-50 is selected due to its superior electrochemical performance than that

of PEGDME-40 and PEGDME-60 (see Figs. S11-S13 for details). Noted that the Zn deposition process is under mass-transport control, so the increase in current can be attributed to increased true electrode surface area.[53, 54] Thus, the current variation can sensitively reflect the change in surface area. As shown in Fig. 2g, the current continuously increases from ~0.05 mA to ~2.1 mA after 1800 s in PEGDME-0, which suggests the rampant 2D diffusion process and would accelerate the formation of Zn dendrites. By contrast, PEGDME-50 maintains a dramatically low current of ~0.04 mA over the whole discharge process, indicating the minimal 2D diffusion and enhanced Zn deposition behavior.[55] This amelioration should be ascribed to preferential surface adsorption of PEGDME on the Zn surface, which serves as a barrier to inhibit lateral diffusion of Zn^{2+} (Fig. S14).[31]

Furthermore, PEGDME-50 brings about decent anti-corrosion capability of Zn. As shown in Fig. S16, Zn foil remains compact structure after immersing in PEGDME-50 for 72 h even under a high temperature of 50 °C, which is significantly better than the porous texture in PEGDME-0 (Figs. 1f-h). The corrosion currents are used to quantificationally compare the corrosion resistance. It shows that the corrosion currents in PEGDME-50 at 0, 25 and 50 °C are one order of magnitude lower than the corresponding values in PEGDME-0 (Fig. 2h). Moreover, a homemade pressure sensor setup is employed to monitor the gas evolution in real-time where Zn foils are immersed in PEGDME-0 and PEGDME-50 (see Fig. S17a for details). Obviously, the pressure is almost constant in PEGDME-50 at 25 °C (Fig. 2i), demonstrating that the side reactions are virtually eliminated. Turning to PEGDME-0, the pressure continually increases after resting 12 h, due to the severe corrosion reaction. Even at 50 °C, PEGDME-50 still presents great effectiveness in suppressing gas generation (Fig. S17b). Similarly, HER during Zn deposition is also restrained in PEGDME-50. ZnO by-products is not detected after depositing Zn in PEGDME-50 even at high

temperature (Fig. S5c), while there are plenty of ZnO in PEGDME-0 under all the temperatures (Fig. 1e). Moreover, the inactive water in PEGDME-50 simultaneously contributes to better electrochemical oxidation stability (Fig. S5d). For example, oxidative decomposition potentials in PEGDME-50 are 2.47 V (25 °C) and 2.17 V (50 °C), which is essentially higher than that in PEGDME-0 (2.27 V at 25 °C and 2.05 V at 50 °C). This would help to realize the high-temperature operation of high-voltage cathodes (e.g., lithium manganese oxide with a charge cut-off voltage of 2.1 V). To sum up, the introduction of PEGDME competitive-solvent into the electrolyte enables the constrained Zn dendrites growth, desirable anti-corrosion property and expanded electrochemical window over a wide temperature range.

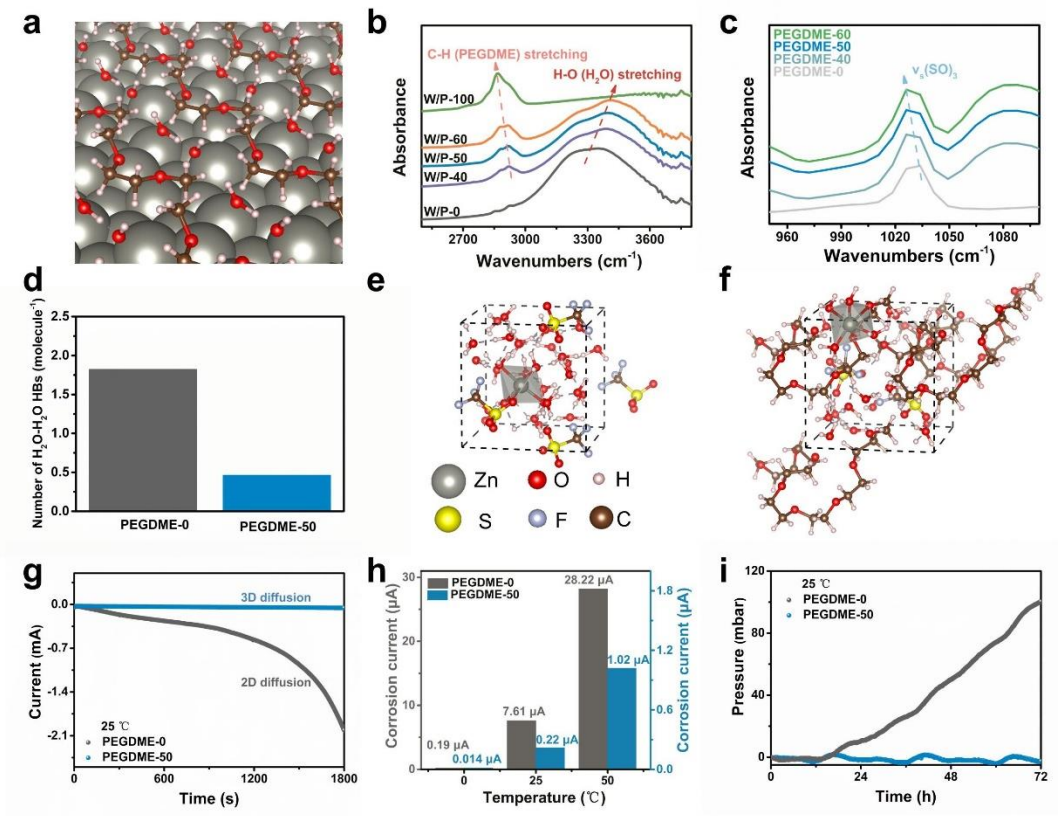

Fig. 2. Experimental and theoretical studies elucidating working mechanism of PEGDME competitive-solvent. (a) Snapshots of AIMD simulations of the surface adsorption structure of Zn

in PEGDME/water solution. Only the species that are directly attached to the Zn surface are shown for clarity. FTIR spectra of (b) H-O stretching (water) in W/P-X and (c) SO_3 symmetric vibration of $Zn(CF_3SO_3)_2$ in PEGDME-X. (d) Average number of HBs formed between H_2O molecules. Snapshots of AIMD simulations of the electrolyte (e) with and (f) without PEGDME. (g) Chronoamperometry under an overpotential of -150 mV at 25 °C. 2D diffusion refers to that the absorbed Zn^{2+} laterally diffuses along the surface to arrive at the most energetically favorable sites for Zn^{2+} reduction. Thus, Zn^{2+} tends to aggregate and grow into dendrites. For 3D diffusion, the absorbed Zn^{2+} would deposit in the near-initial adsorption sites with constrained 2D surface diffusion, which helps to increase nucleation sites and realize improved Zn deposition morphologies. (h) Corrosion currents derived from linear polarization experiments in PEGDME-0 and PEGDME-50 at 0, 25 and 50 °C (i) Pressure evolution in real-time when Zn foils are immersed in the two electrolytes at 25 °C.

3.3 Dendrite-free morphologies in PEGDME-50.

To examine the Zn deposition/stripping behavior, the SEM images under various Zn deposition capacities are acquired in PEGDME-0 and PEGDME-50 at different temperatures (Fig. 3 and Figs. S3 and S18). For PEGDME-0, the uneven morphologies with massive protuberances are observed at 0 °C after depositing 0.1, 0.5 and 1 mAh/cm^2 of Zn. Although the nonuniform deposition is slightly alleviated with raised temperature (25 and 50 °C), the loose and rough structures still prevail at all deposition capacity. These phenomena agree well with the significantly augmented current in CA tests (Fig. 2g), which is detrimental to the electrochemical performance. On the contrary, the deposited Zn metal of 0.1 mAh/cm^2 is smooth and compact in PEGDME-50 at all the test temperatures, i.e., 0, 25 and 50 °C (Figs. S18a-f). The Zn dendrite-free morphologies maintain when deposition capacity increases to 0.5 and 1 mAh/cm^2 (Figs. 3g-l). The corresponding optical

photos are consistent with the microscopic structures of SEM images. Specifically, the dense and uniform Zn metal is observed in PEGDME-50 (Fig. S19), while PEGDME-0 shows randomly deposited Zn.

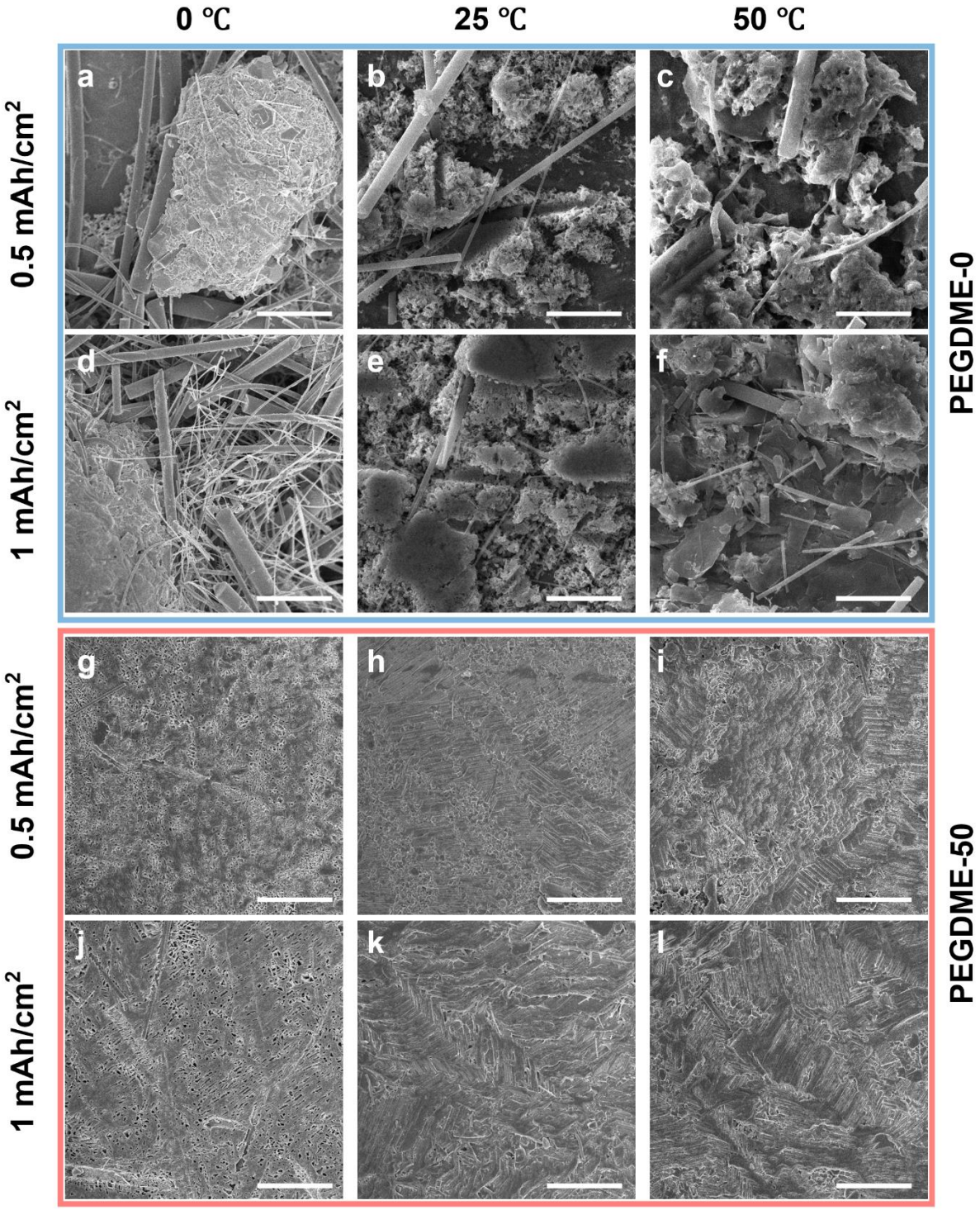

Fig. 3. Morphological characterization of Zn deposition at 1 mA/cm^2. Zn deposition of 0.5 mAh/cm^2 in PEGDME-0 at (a) 0 °C, (b) 25 °C and (c) 50 °C, and 1 mAh/cm^2 at (d) 0 °C, (e) 25 °C and (f) 50 °C. Zn deposition of 0.5 mAh/cm^2 in PEGDME-50 at (g) 0 °C, (h) 25 °C and (i) 50 °C, and 1 mAh/cm^2 at (j) 0 °C, (k) 25 °C and (l) 50 °C. The scale bar is 10 μm.

3.4 Wide-temperature performance in PEGDME-50

To further verify the superior of PEGDME-50, the cycle and CE performance are respectively evaluated using Zn/Zn and Cu/Zn cells at 0, 25 and 50 °C. As shown in Fig. 4b, Zn/Zn cells could safely run for 2000 h in PEGDME-50 at 25 °C (1 mA/cm^2 and 1 mAh/cm^2), which is over tenfold longer than that in PEGDME-0 (~175 h), although the former has slightly higher overpotential (see Fig. S5e for details). In the absence of PEGDME competitive-solvent, the cycle life is further reduced, i.e., ~55 h at 0 °C and 100 h at 50 °C, owing to the excessive dendrite growth (0 °C) and parasitic reactions (50 °C) compared with room temperature (Figs. 4a and c). Surprisingly, the exceptional Zn deposition/stripping life of 2000 h and 1600 h are respectively achieved in PEGDME-50 at 0 °C and 50 °C. Similar enhancements persist in PEGDME-50 when current density and cycling capacity are respectively increased to 3 mA/cm^2 and 3 mAh/cm^2. Specifically, the cell could deliver a stable cycle life of more than 380 h in PEGDME-50 over a wide temperature range from -0 to 50 °C (Fig. S20), while a short circuit is observed after only ~25 h in PEGDME-0 at all the tested temperatures. For CE tests, the Cu/Zn cells only survive dozens of cycles in PEGDME-0 at 0, 25 and 50 °C (Figs. 4d-f). Conversely, PEGDME-50 could deliver the fair CE for more than 1000 cycles at these three temperatures under the same condition. The average CEs are 99.5% at 0 °C, 99.2% at 25 °C and 97.9% at 50 °C. Pushing to the limit, we exploit the Zn/Zn cells and Cu/Zn cells even at -15 °C and 65 °C, where PEGDME-50 enables

stable plating/stripping and high CEs at these temperature extremes. (Fig. S21). By contrast, the cells fail

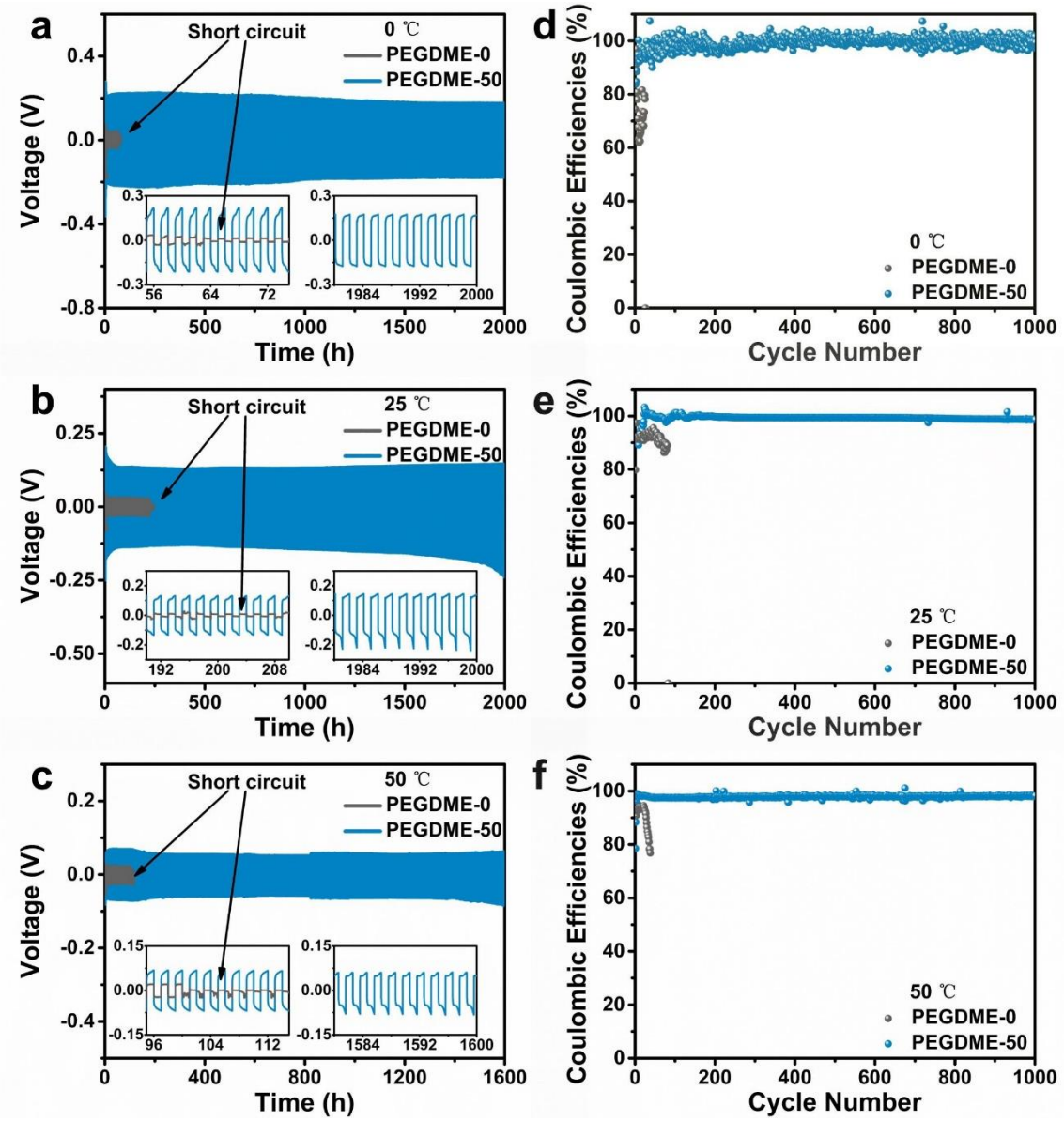

Fig. 4. The electrochemical performance of Zn metal anodes at different temperatures. The cycle performance (1 mA/cm^2 and 1 mAh/cm^2) of Zn/Zn cells at (a) 0 °C, (b) 25 °C and (c) 50 °C, and CE performance (1 mA/cm^2 and 1 mAh/cm^2) of Cu/Zn cells at (d) 0 °C, (e) 25 °C and (f) 50 °C in PEGDME-0 and PEGDME-50.

to operate in PEGDME-0 at -15 °C owing to the frozen electrolyte (Fig. S22) and suffer from rapid failure at 65 °C due to dramatic side reactions. These improvements are in line with the previous discussions (Fig. 2) showing the beneficial effects of the PEGDME competitive-solvent to circumvent the mutually interferential issues of the dendrites growth, corrosion and HER. Note that the PEGDME could be partially consumed due to the encapsulation in the Zn deposition layer during cycling, which is the main reason for the performance deterioration after long-term cycles (see Figs. S23-S25 for details).

To evaluate the feasibility of PEGDME-50 in real Zn metal systems, the full cells paired with a commercial V_2O_5 cathode are tested at various temperatures. The cells present a high specific capacity of ~103.9 mAh/g for 600 cycles in PEGDME-50 at 25 °C, while the capacity rapidly degrades to 79.2 mAh/g after only 200 cycles in PEGDME-0 (Fig. 5b). Impressive stability still maintains in PEGDME-50 at 0 °C and 50 °C (Figs. 5a and c). Specifically, it displays a high capacity of 77.8 mAh/g after 1000 cycles at 0 °C and 81.5 mAh/g after 200 cycles at 50 °C, which much outperforms the performance in PEGDME-0. It is worth mentioning that PEGDME-50 allows the cells to cycle at an even lower temperature of -15 °C and a higher one of 65 °C (Fig. S26), which agrees well with the results of Zn/Zn and Cu/Zn cells under the same temperatures (Fig. S21). These prominent enhancements in PEGDME-50 are ascribed to the delightful Zn deposition/stripping, as verified by the SEM images of cycled Zn metal anodes (Figs. 5g and h and Figs. S27 and S28). Smooth and uniform morphologies are observed in PEGDME-50 at 0, 25 and 50 °C, whereas Zn metal shows a porous and rough structure in PEGDME-0. Although the increased Zn plating/stripping overpotential due to PEGDME addition would be detrimental to the discharge voltage under the full cell, the adverse effect is overturned by the significantly improved cyclic stability and safety.

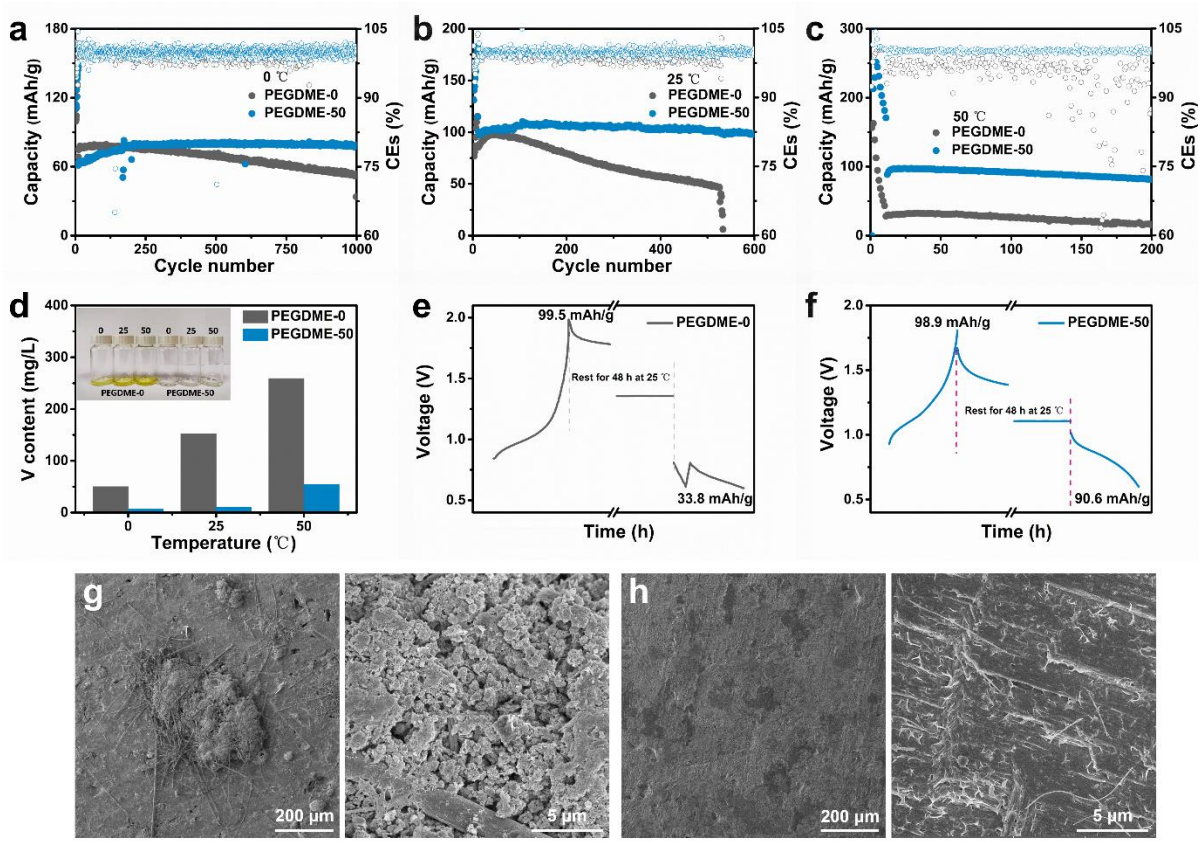

Fig. 5. The electrochemical behavior of full cells and decent compatibility for cathode under thermal extremes. The cycle performance of Zn/V_2O_5 full cells in PEGME-0 and PEGDME-50 at (a) 0 °C, (b) 25 °C and (c) 50 °C. (d) Vanadium element content in PEGDME-0 and PEGDME-50 where V_2O_5 cathode is soaked for 2 days at various temperatures. The self-discharge performance of Zn/V_2O_5 full cells in (e) PEGDME-0 and (f) PEGDME-50 at 25 °C. The SEM images of Zn metal anodes after 50 cycles in full cells using (g) PEGDME-0 and (h) PEGDME-50 at 25 °C.

For the completeness of this work, we explore the effect of PEGDME addition on the cathode. Thanks to the reduced water activities, the dissolution of V_2O_5 cathode is essentially inhibited, as

verified by the inductively coupled plasma mass spectrometry (ICP-MS).[56] The samples are prepared by immersing V_2O_5 cathode in PEGDME-0 and PEGDME-50 for 2 days at 0, 25 and 50 °C. As shown in Fig. 5d, the concentration of vanadium in PEGDME-0 is 50.1 mg/L at 0 °C, and then increased to 152.0 mg/L (25 °C) and 259.0 mg/L (50 °C). On the contrary, the PEGDME competitive-solvent gives rise to much lower concentrations (6.72 mg/L, 10.6 mg/L and 54.4 mg/L respectively at 0, 25, and 50 °C). The compatibility between V_2O_5 cathode and PEGDME-50 is further proved through self-discharge measurements, where cells are cycled for 50 cycles and then rested 48 h under charge state before further discharge. At 25 °C, the discharge-to-charge capacity ratio is merely 34.0% in PEGDME-0 due to the severe self-discharge (Fig. 5e). By contrast, cells present a much lower self-discharge rate with a high discharge-to-charge capacity of 91.6% in PEGDME-50 under the same temperature (Fig. 5f). A similar phenomenon is observed at 0 and 50°C, (Fig. S29). Moreover, it is found that the expanded electrochemical window of PEGDME-50 is beneficial to realizing high-voltage cathode even at high temperatures (Fig. S30). Namely, the full cells coupled with $LiMn_2O_4$ cathode are stably cycled between 1.4 and 2.1 V in PEGDME-50 at 25 °C and 50 °C. Although such full cells could run at 25 °C in PEGDME-0, its voltage cannot reach 2.1 V at 50 °C due to the uncontrollable water decomposition, consistent with the results on the electrochemical window (Fig. S5d). These results demonstrate that PEGDME-50 could concurrently stabilize Zn anodes and cathodes, enabling durable Zn metal batteries at various temperatures.

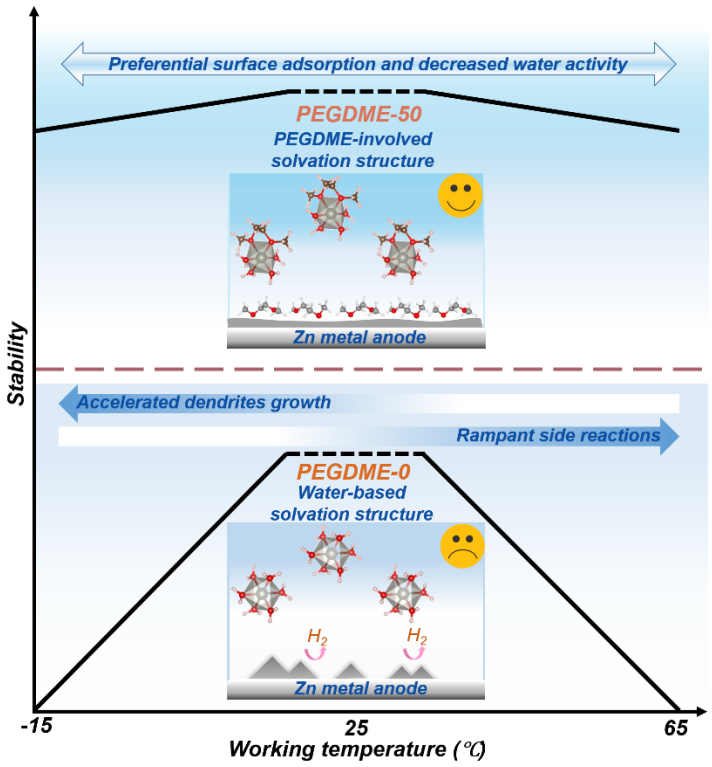

Fig. 6. Illustration of thermal instability of Zn metal anodes in PEGDME-0 and highly improved stability in PEGDME-50. For PEGDME-0, low temperature causes accelerated dendrites growth and high one renders rampant side reactions. Multifunctional PEGDME-50 is proposed to enable stable wide-temperature Zn metal batteries.

4. Conclusions

We explore Zn deposition/stripping behavior under thermal extremes and reveal that unstable Zn plating/stripping roots exacerbate dendrite growth and side reactions (Fig. 6). These revealed temperature-induced challenges could be regarded as explicit guidelines for stabilizing Zn deposition/stripping under thermal extremes. For instance, we show here the primary issue associated with the performance of Zn metal anode at high temperatures is the parasitic reactions instead of dendrite formation. A multifunctional oligomer PEGDME is then proposed as

competitive-solvent to circumvent these issues over a wide temperature range. The complementary experimental and theoretical results demonstrate the following assets of the competitive-solvent: First, its preferential surface adsorption than water molecules on Zn metal could restrain dendrites formation and corrosion. Besides, it could re-construct HBs with water and participate in the solvation structure of Zn^{2+}, which respectively weaken both water/water and water/Zn^{2+} interaction for alleviating parasitic reactions even at high temperatures. As a result, Zn dendrite-free morphologies and a remarkably prolonged lifetime of more than 1600 h are achieved with PEGDME-50 at 0, 25 and 50 °C. Furthermore, the deceased water activities in PEGDME-50 lead to the suppressed dissolution of cathode and expanded electrochemical window, hence realizing Zn/V_2O_5 batteries over a wide temperature range from -15 to 65 °C and stable high-voltage Zn/$LiMn_2O_4$ batteries at elevated temperatures. This work not only offers a fundamental understanding of the Zn deposition/stripping behavior under thermal extremes but also provides an avenue for constructing reliable wide-temperature Zn metal batteries by manipulating the electrode/electrolyte interface and solvation chemistry interface and solvation.

References

[1] D. Chao, W. Zhou, F. Xie, C. Ye, H. Li, M. Jaroniec, S.Z. Qiao, Sci Adv, 6 (2020) eaba4098.
[2] W. Du, E.H. Ang, Y. Yang, Y. Zhang, M. Ye, C.C. Li, Energy & Environmental Science, 13 (2020) 3330-3360.
[3] T. Zhang, Y. Tang, S. Guo, X. Cao, A. Pan, G. Fang, J. Zhou, S. Liang, Energy & Environmental Science, 13 (2020) 4625-4665.
[4] F. Wan, X. Zhou, Y. Lu, Z. Niu, J. Chen, ACS Energy Letters, 5 (2020) 3569-3590.
[5] Y. Yin, S. Wang, Q. Zhang, Y. Song, N. Chang, Y. Pan, H. Zhang, X. Li, Adv Mater, 32 (2020) e1906803.
[6] S.B. Wang, Q. Ran, R.Q. Yao, H. Shi, Z. Wen, M. Zhao, X.Y. Lang, Q. Jiang, Nat Commun, 11 (2020) 1634.
[7] N. Zhang, S. Huang, Z. Yuan, J. Zhu, Z. Zhao, Z. Niu, Angew Chem Int Ed Engl, (2020).
[8] Z. Ye, Z. Cao, M.O. Lam Chee, P. Dong, P.M. Ajayan, J. Shen, M. Ye, Energy Storage Materials, 32 (2020) 290-305.
[9] C. Xie, Y. Li, Q. Wang, D. Sun, Y. Tang, H. Wang, Carbon Energy, 2 (2020) 540-560.
[10] J. Shin, J. Lee, Y. Park, J.W. Choi, Chem Sci, 11 (2020) 2028-2044.
[11] N. Zhang, X. Chen, M. Yu, Z. Niu, F. Cheng, J. Chen, Chem Soc Rev, 49 (2020) 4203-4219.
[12] Q. Zhang, J. Luan, Y. Tang, X. Ji, H. Wang, Angew Chem Int Ed Engl, 59 (2020) 13180-13191.
[13] Z. Cai, Y. Ou, J. Wang, R. Xiao, L. Fu, Z. Yuan, R. Zhan, Y. Sun, Energy Storage Materials, 27 (2020) 205-211.
[14] S. Chen, R. Lan, J. Humphreys, S. Tao, Energy Storage Materials, 28 (2020) 205-215.
[15] J. Hao, X. Li, X. Zeng, D. Li, J. Mao, Z. Guo, Energy & Environmental Science, 13 (2020) 3917-3949.
[16] Y. Zeng, X. Zhang, R. Qin, X. Liu, P. Fang, D. Zheng, Y. Tong, X. Lu, Adv Mater, 31 (2019) e1903675.
[17] N. Wang, X. Dong, B. Wang, Z. Guo, Z. Wang, R. Wang, X. Qiu, Y. Wang, Angew Chem Int Ed Engl, 59 (2020) 14577-14583.
[18] N. Wang, Y. Yang, X. Qiu, X. Dong, Y. Wang, Y. Xia, ChemSusChem, 13 (2020) 5556-5564.
[19] A. Naveed, H. Yang, Y. Shao, J. Yang, N. Yanna, J. Liu, S. Shi, L. Zhang, A. Ye, B. He, J. Wang, Adv Mater, 31 (2019) e1900668.
[20] A. Bayaguud, X. Luo, Y. Fu, C. Zhu, ACS Energy Letters, 5 (2020) 3012-3020.
[21] Y. Tang, C. Liu, H. Zhu, X. Xie, J. Gao, C. Deng, M. Han, S. Liang, J. Zhou, Energy Storage Materials, 27 (2020) 109-116.
[22] F. Wang, O. Borodin, T. Gao, X. Fan, W. Sun, F. Han, A. Faraone, J.A. Dura, K. Xu, C. Wang, Nat Mater, 17 (2018) 543-549.
[23] C. Han, W. Li, H.K. Liu, S. Dou, J. Wang, Nano Energy, 74 (2020).
[24] D. Han, S. Wu, S. Zhang, Y. Deng, C. Cui, L. Zhang, Y. Long, H. Li, Y. Tao, Z. Weng, Q.H. Yang, F. Kang, Small, 16 (2020) e2001736.
[25] J. Cong, X. Shen, Z. Wen, X. Wang, L. Peng, J. Zeng, J. Zhao, Energy Storage Materials, 35 (2021) 586-594.
[26] C. Li, X. Shi, S. Liang, X. Ma, M. Han, X. Wu, J. Zhou, Chemical Engineering Journal, 379 (2020).

[27] Z. Kang, C. Wu, L. Dong, W. Liu, J. Mou, J. Zhang, Z. Chang, B. Jiang, G. Wang, F. Kang, C. Xu, ACS Sustainable Chemistry & Engineering, 7 (2019) 3364-3371.
[28] R. Qin, Y. Wang, M. Zhang, Y. Wang, S. Ding, A. Song, H. Yi, L. Yang, Y. Song, Y. Cui, J. Liu, Z. Wang, S. Li, Q. Zhao, F. Pan, Nano Energy, 80 (2021).
[29] H. Qiu, X. Du, J. Zhao, Y. Wang, J. Ju, Z. Chen, Z. Hu, D. Yan, X. Zhou, G. Cui, Nat Commun, 10 (2019) 5374.
[30] Y. Jin, K.S. Han, Y. Shao, M.L. Sushko, J. Xiao, H. Pan, J. Liu, Advanced Functional Materials, 30 (2020).
[31] A. Mitha, A.Z. Yazdi, M. Ahmed, P. Chen, ChemElectroChem, 5 (2018) 2409-2418.
[32] S.J. Banik, R. Akolkar, Journal of The Electrochemical Society, 160 (2013) D519-D523.
[33] M. Cui, Y. Xiao, L. Kang, W. Du, Y. Gao, X. Sun, Y. Zhou, X. Li, H. Li, F. Jiang, C. Zhi, ACS Applied Energy Materials, 2 (2019) 6490-6496.
[34] Z. Hou, Y. Gao, H. Tan, B. Zhang, Nat Commun, 12 (2021) 3083.
[35] J. Hao, L. Yuan, C. Ye, D. Chao, K. Davey, Z. Guo, S. Qiao, Angew Chem Int Ed Engl, (2021).
[36] N. Chang, T. Li, R. Li, S. Wang, Y. Yin, H. Zhang, X. Li, Energy & Environmental Science, 13 (2020) 3527-3535.
[37] Q. Zhang, Y. Ma, Y. Lu, L. Li, F. Wan, K. Zhang, J. Chen, Nat Commun, 11 (2020) 4463.
[38] Z. Lu, J. Liu, F. Ciucci, Energy Storage Materials, 28 (2020) 146-152.
[39] Z. Hou, H. Tan, Y. Gao, M. Li, Z. Lu, B. Zhang, Journal of Materials Chemistry A, 8 (2020) 19367-19374.
[40] X. Hua, A.S. Eggeman, E. Castillo-Martinez, R. Robert, H.S. Geddes, Z. Lu, C.J. Pickard, W. Meng, K.M. Wiaderek, N. Pereira, G.G. Amatucci, P.A. Midgley, K.W. Chapman, U. Steiner, A.L. Goodwin, C.P. Grey, Nat Mater, (2021).
[41] T.H. Dunning Jr, The Journal of chemical physics, 90 (1989) 1007-1023.
[42] P.J. Stephens, F.J. Devlin, C.F. Chabalowski, M.J. Frisch, The Journal of physical chemistry, 98 (1994) 11623-11627.
[43] F. Neese, Rev.: Comput. Mol. Sci, 2 (2012) 73-78.
[44] A.D. Becke, The Journal of chemical physics, 98 (1993) 1372-1377.
[45] M. Segall, P.J. Lindan, M.a. Probert, C.J. Pickard, P.J. Hasnip, S. Clark, M. Payne, Journal of physics: condensed matter, 14 (2002) 2717.
[46] J. Hafner, Journal of computational chemistry, 29 (2008) 2044-2078.
[47] J.P. Perdew, K. Burke, M. Ernzerhof, Physical review letters, 77 (1996) 3865.
[48] X.B. Cheng, R. Zhang, C.Z. Zhao, Q. Zhang, Chem Rev, 117 (2017) 10403-10473.
[49] J. Shim, R. Kostecki, T. Richardson, X. Song, K.A. Striebel, Journal of Power Sources, 112 (2002) 222-230.
[50] C. Barchasz, J.-C. Leprêtre, S. Patoux, F. Alloin, Electrochimica Acta, 89 (2013) 737-743.
[51] J. Xie, Z. Liang, Y.C. Lu, Nat Mater, 19 (2020) 1006-1011.
[52] M.Z. Jora, M.V.C. Cardoso, E. Sabadini, Journal of Molecular Liquids, 222 (2016) 94-100.
[53] C.J. Lan, C.Y. Lee, T.S. Chin, Electrochimica Acta, 52 (2007) 5407-5416.
[54] J.M. Wang, L. Zhang, C. Zhang, J.Q. Zhang, Journal of Power Sources, 102 (2001) 139-143.
[55] Z. Zhao, J. Zhao, Z. Hu, J. Li, J. Li, Y. Zhang, C. Wang, G. Cui, Energy & Environmental Science, 12 (2019) 1938-1949.
[56] J.Q. Huang, X. Guo, X. Lin, Y. Zhu, B. Zhang, Research, 2019 (2019) 2635310.